Heliyon 9 (2023) e21739

Contents lists available at ScienceDirect

Heliyon

journal homepage: www.cell.com/heliyon

The synergistic triad of graphene quantum dots, polymer, and ferrites for the photodegradation of dyes in aqueous solution

Saima Perveen [a], Waheed Miran [b], Gajanan Ghodake [c], Waqar Azeem [d], Xizi Long [e], Fahad Azad [a,*]

[a] School of Natural Sciences (SNS), National University of Sciences and Technology (NUST), Islamabad, 44000, Pakistan
[b] Department of Chemical Engineering, School of Chemical and Materials Engineering, National University of Sciences and Technology, Islamabad, 44000, Pakistan
[c] Department of Biological and Environmental Science, Dongguk University-Seoul, Ilsandong, Goyang, 10326, Gyeonggi, South Korea
[d] Faculty of Resilience, Rabdan Academy, Abu Dhabi, United Arab Emirates
[e] The Key Laboratory of Typical Environmental Pollution and Health Hazards of Hunan Province, School of Public Health, Hengyang Medical School, University of South China, Hengyang, 421001, China

ARTICLE INFO

Keywords:
Mg-$ZnFe_2O_4$
Graphene quantum dots (GQDs)
Ternary nanocomposite
Methylene blue (MB)
Crystal violet (CV)
Photocatalytic degradation

ABSTRACT

This work aimed to investigate photocatalytic properties of GQDs@PEG@Mg–$ZnFe_2O_4$ nanocomposite, composed of graphene quantum dots (GQDs), polyethylene glycol (PEG), and Mg–$ZnFe_2O_4$, for the degradation of methylene blue (MB) and crystal violet (CV). This nanocomposite was synthesized using facile ultrasonics-assisted methodology. XRD analysis confirmed the formation of the spinel structure of the Mg–$ZnFe_2O_4$ in the nanocomposite, whereas the presence of GQDs and PEG was confirmed by Fourier transform infrared spectroscopy. Scanning electron microscopy (SEM) revealed a reduction in agglomeration and particle size in the ternary nanocomposite. The GQDs@PEG@Mg–$ZnFe_2O_4$ nanocomposite demonstrates a remarkable degradation efficiency of 98 % for CV and MB dyes in the presence of sunlight in 120 min, indicating its potential as an efficient photocatalyst. Vibrating sample magnetometer (VSM) analysis confirmed the superparamagnetic behavior of the GQDs@PEG@Mg–$ZnFe_2O_4$ nanocomposite which enables magnetic recovery of the photocatalyst after the degradation process. Overall, this study emphasizes the utilization of an environmentally friendly approach to effectively eliminate organic pollutants from wastewater, addressing a crucial environmental concern.

1. Introduction

The increasing concern over environmental pollution caused by pollutants such as solid wastes and dyes has led to a growing interest in the development of efficient and environment-friendly techniques for their removal [1–3]. Photocatalytic degradation has emerged as a promising approach, utilizing light energy to drive chemical reactions that decompose the dyes into less harmful products. Among various photocatalysts, zinc oxide (ZnO) and titanium dioxide (TiO_2) have been widely studied and utilized for their photocatalytic properties [4–7]. However, their limitations in terms of low efficiency, poor stability, and limited response to visible light have led to the search for alternative photocatalysts with improved performance. Recently, ferrites have caught attraction as a

---

[*] Corresponding author.
E-mail address: fahad.azad@sns.nust.edu.pk (F. Azad).

https://doi.org/10.1016/j.heliyon.2023.e21739
Received 21 August 2023; Received in revised form 20 October 2023; Accepted 26 October 2023

photocatalyst due to their capability to absorb visible light. Additionally, their magnetic recoverability after the degradation process, cost-effectiveness, and non-toxic nature make them superior in contrast to conventional photocatalysts [8]. Furthermore, the chemical stability of ferrites enables their use in harsh conditions, further expanding their utility.

Among ferrites, Mg–$ZnFe_2O_4$ has gained much attraction because of its high stability, facile synthesis, and diverse applications in fields such as energy harvesting, sensors, catalysis, high frequency, and biomedical applications [9–11]. Mg–$ZnFe_2O_4$ is a promising ferrite with optimal potential for photocatalytic activity [12], which enables it to effectively generate and transfer electrons and holes, leading to more efficient degradation of dyes.

GQDs are reported to have a tunable bandgap in the visible light spectrum [13]. When exposed to sunlight, GQDs have the dual tendency to serve both as a source and acceptor of electrons. Qu et al. have explored the potential of GQDs in enhancing the photocatalytic performance of TiO_2 in GQDs/TiO_2 nanocomposite, in contrast to pure TiO_2. The enhanced photocatalytic activity from 51 % to 92 % in GQDs/TiO_2 nanocomposite was attributed to up-conversion properties of the GQDs, increased photogenerated electron-hole separation and efficient visible light absorption [13]. Sarwar et al. have studied $CuWO_4$/GQDs photocatalyst for visible light degradation of phenol. Results revealed an enhancement in the photocatalytic activity from 19 % to 54 % for $CuWO_4$ and $CuWO_4$/GQDs nanocomposite, respectively. This improvement in the photocatalytic activity was linked to the efficient charge transfer (electrons) from $CuWO_4$ to GQDs [14]. Khan et al. have explored the potential of photocatalyst GQD-0.1Fe–TiO_2-300 in comparison to pure 0.1Fe–TiO_2-300 for decolorizing RB5 dye in textile wastewater. The addition of GQDs resulted in the photocatalytic decolorization from 95 % to 97 % with no impact on seed germination of L. esculentum [15]. These studies indicate that incorporating GQDs into magnesium-zinc ferrite can help in the amplification of Mg–$ZnFe_2O_4$ photocatalytic performance.

Regardless of these properties, magnetic materials have a tendency to aggregate which adversely affects the degradation efficiency. To prevent aggregation, researchers have utilized the incorporation of magnetic ferrite matrix into porous and layered materials. Tabit et al. studied agglomeration tendency of $CoFe_2O_4$ nanoparticles by manipulating its structure with porous GO. The reduction in the agglomeration of the particles was associated to the degradation efficiency of rhodamine B [16]. Yang et al. controlled the agglomeration of Fe_3O_4 nanoparticles by embedding it into a polymer matrix (PANI). Fe_3O_4/PANI nanocomposite showed a significant improvement in photocatalytic activity due to less agglomeration and enhanced light absorption of sunlight [17]. Thus, performance of a photocatalyst can be enhanced by combining the GQDs and a polymer with ferrites. In this work, we synthesized a ternary nanocomposite based on graphene quantum dots (GQDs), polyethylene glycol (PEG), and magnesium-zinc ferrites. The ternary nanocomposite possesses a unique combination of properties that provides a condensed approach to overcome these issues. GQDs improve the conductivity of the ternary nanocomposite which facilitates better charge transfer for the photocatalytic process. Moreover, GQDs are known to possess excellent visible light absorption, enabling more effective utilization of the solar spectrum. Whereas polyethylene glycol in the nanocomposite acts as a stabilizing agent, reducing the agglomeration of the photocatalyst. The hydrophilic nature of PEG helps in improving the water solubility of the nanocomposite which is particularly important for efficient degradation of water-soluble dyes. The presence of PEG in the ternary nanocomposite results in better dispersion and improved photocatalytic activity.

This study investigates the photocatalytic degradation of widely used dyes, methylene blue and crystal violet, employing a ternary GQDs@PEG@Mg–ZnFe2O4 nanocomposite. These are widely used dyes in textile and printing industries and cause environmental pollution when discharged in wastewater. Ternary GQDs@PEG@Mg–$ZnFe_2O_4$ nanocomposite was synthesized through a facile sonication-assisted process, followed by comprehensive characterizations by various techniques, including X-ray diffraction (XRD), scanning electron microscopy (SEM), ultraviolet–visible spectrophotometry (UV–Vis), Fourier transform infrared spectroscopy (FTIR) and vibrating sample magnetometry (VSM). The synthesized nanocomposite exhibited remarkable photocatalytic activity for the degradation of both methylene blue and crystal violet under sunlight with efficient reaction kinetics. These findings hold significant potential for the development of efficient and eco-friendly approaches to tackle dye removal from wastewater.

2. Experimental

2.1. Materials

Mg–$ZnFe_2O_4$ was synthesized using the sol-gel method. All the precursors: $Mg(NO_3)_2{\bullet}6H_2O$, $Zn(NO_3)_2{\bullet}6H_2O$, $Fe(NO_3)_3{\bullet}9H_2O$, and $C_6H_8O_7$ were purchased from Sigma Aldrich.

2.2. Synthesis

2.2.1. Graphene quantum dots (GQDs)

The synthesis of GQDs was performed through direct pyrolysis of $C_6H_8O_7$. The complete method of the synthesis process is reported elsewhere [18].

2.2.2. Mg–$ZnFe_2O_4$

The sol-gel method was employed to synthesize Mg–$ZnFe_2O_4$. A 0.5 M aqueous solution of $Mg(NO_3)_2{\bullet}6H_2O$ and a 0.5 M aqueous solution of $Zn(NO_3)_2{\bullet}6H_2O$ were combined with a 2 M aqueous solution of $Fe(NO_3)_3{\bullet}9H_2O$ while stirring constantly. The chelating agent ($C_6H_8O_7$) was introduced in the above solution after 30 min of stirring. The solution was then kept at 90 °C with steady stirring for ~5 h. A crimson gel was obtained which was subsequently dried at 150 °C. Finally, Mg–$ZnFe_2O_4$ was acquired by the calcination of the above product at 1000 °C in a muffle furnace for 4 h.

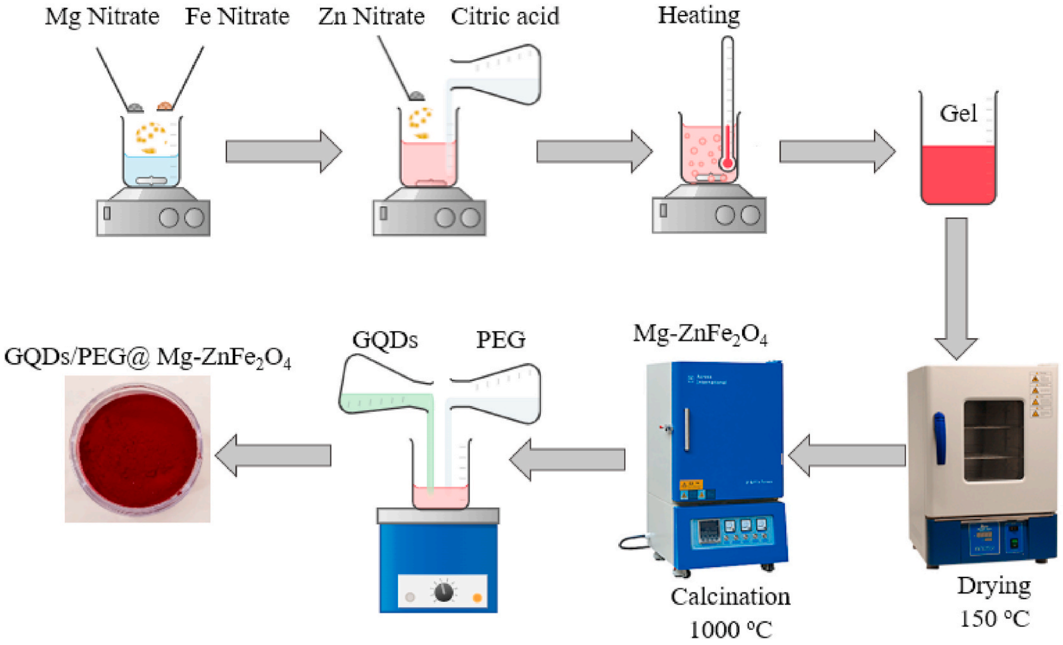

Fig. 1. The synthesis of the ternary GQDs@PEG@Mg–ZnFe$_2$O$_4$ nanocomposite.

2.2.3. GQDs@Mg–ZnFe$_2$O$_4$ and PEG@Mg–ZnFe$_2$O$_4$

The binary nanocomposite was synthesized using the ultrasonication method. 0.5 g of pre-synthesized Mg–ZnFe$_2$O$_4$ was dissolved in 20 ml of deionized water and subjected to sonication for 2 h separately. 5 ml of GQDs and PEG (200) solution were mixed in the above solution separately and kept for further sonication (2 h). The resultant solutions were then dried at 100 °C in an oven to obtain the final binary nanocomposite of GQDs@Mg–ZnFe$_2$O$_4$ and PEG@Mg–ZnFe$_2$O$_4$, respectively.

2.2.4. GQDs@PEG@Mg–ZnFe$_2$O$_4$

0.5 g of pre-synthesized Mg–ZnFe$_2$O$_4$ was dissolved in 20 ml of deionized water and subjected to ultrasonication for 2 h. 5 ml of GQDs and PEG solution were added in the above solution and kept for further sonication (2 h) before undergoing drying at 150 °C in an oven, resulting in the formation of the GQDs@PEG@Mg–ZnFe$_2$O$_4$ ternary nanocomposite. Fig. 1 presents a schematic of the overall synthesis procedure of GQDs@PEG@Mg–ZnFe$_2$O$_4$.

The structural properties were characterized using X-ray diffraction with a Cu-kα beam (Bourevestnik, DRON-8). The presence of different vibrational bands in the synthesized nanocomposite was analyzed using FTIR spectra (Lamda 365). The morphological properties were analyzed using scanning electron microscopy (SEM JEOL JSM-6390) and the magnetic properties were disclosed through vibrating sample magnetometry (DXV-220, Dexing).

3. Results and discussions

3.1. X-ray diffraction (XRD)

The structural properties of as-synthesized samples were characterized by X-ray diffraction analysis at room temperature. The X-ray diffractograms were obtained for all the samples: Mg–ZnFe$_2$O$_4$, GQDs@Mg–ZnFe$_2$O$_4$, PEG@Mg–ZnFe$_2$O$_4$, and GQDs@PEG@Mg–ZnFe$_2$O$_4$ and illustrated in Fig. 1(A). The XRD patterns of Mg–ZnFe$_2$O$_4$ showed distinct peaks at (111), (220), (311), (400), (422), (511), (440), and (533), indicating the cubic structure of the prepared sample. These peaks are in accordance with JCPDS-22-1012. The relatively higher intensity of (220), (311), (440), and (511) peaks indicate the preferential growth along these planes in all samples [19]. The absence of any secondary peak and high signal-to-noise ratio confirmed the purity and high crystallinity in all the samples. A slight hump appeared at $2\theta \sim 20^\circ$ in GQDs@Mg–ZnFe$_2$O$_4$ which can be attributed to the unique (002) peak of GQDs. The characteristic peak of GQDs indicates the presence of GQDs in Mg–ZnFe$_2$O$_4$, which is in accordance with the literature [18]. A decrease in the intensities of the Mg–ZnFe$_2$O$_4$ phase in PEG@Mg–ZnFe$_2$O$_4$ was observed without any other characteristic peaks, suggesting that PEG is dispersed randomly throughout the structure rather than forming a crystalline phase. Similarly, GQDs@PEG@Mg–ZnFe$_2$O$_4$ showed the peaks of GQDs and Mg–ZnFe$_2$O$_4$ with the amorphous nature of PEG in the ternary composite [20,21].

Williamson-Hall model was used to evaluate microstructural properties of the synthesized samples which relates broadening of the diffraction peaks with the microstrain and crystallite size. The contribution to total peak broadening (β_{tot}) due to crystallite size (β_c) and lattice microstrain (β_s) is given as:

Table 1
Structural parameters of $Mg–ZnFe_2O_4$, $GQDs@Mg–ZnFe_2O_4$, $PEG@Mg–ZnFe_2O_4$, and $GQDs@PEG@Mg–ZnFe_2O_4$ samples.

Samples	ε ($X10^{-3}$)	D (nm)	a (Å)	V ($Å^3$)	d (Å)	d_X $(\frac{g}{cm^3})$
$Mg–ZnFe_2O_4$	2.11	43	8.436	600	2.543	4.78
$GQDs@Mg–ZnFe_2O_4$	2.28	47	8.430	599	2.541	4.88
$PEG@Mg–ZnFe_2O_4$	1.25	30	8.425	598	2.540	4.89
$GQDs@PEG@Mg–ZnFe_2O_4$	1.58	10	8.418	596	2.538	4.91

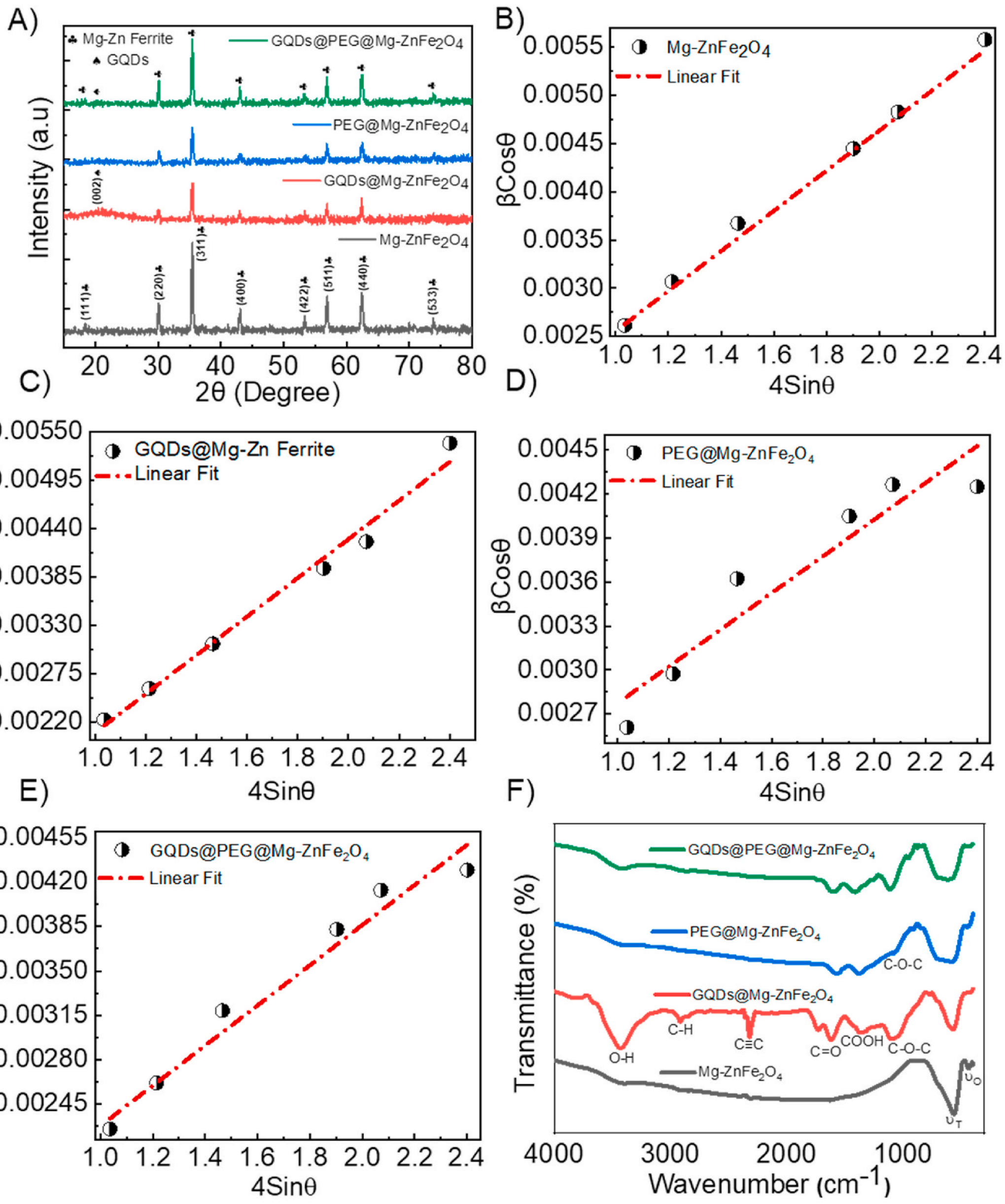

Fig. 2. (A) XRD pattern (B–E) WH plots (F) FTIR spectra of $Mg–ZnFe_2O_4$, $GQDs@Mg–ZnFe_2O_4$, $PEG@Mg–ZnFe_2O_4$, and $GQDs@PEG@Mg–ZnFe_2O_4$ nanocomposites.

$$\beta_{tot} = \beta_c + \beta_s = \frac{\kappa\,\lambda}{D cos\theta} + 4\left(\frac{\Delta d_{hkl}}{d_{hkl}}\right) tan\,\theta \tag{1}$$

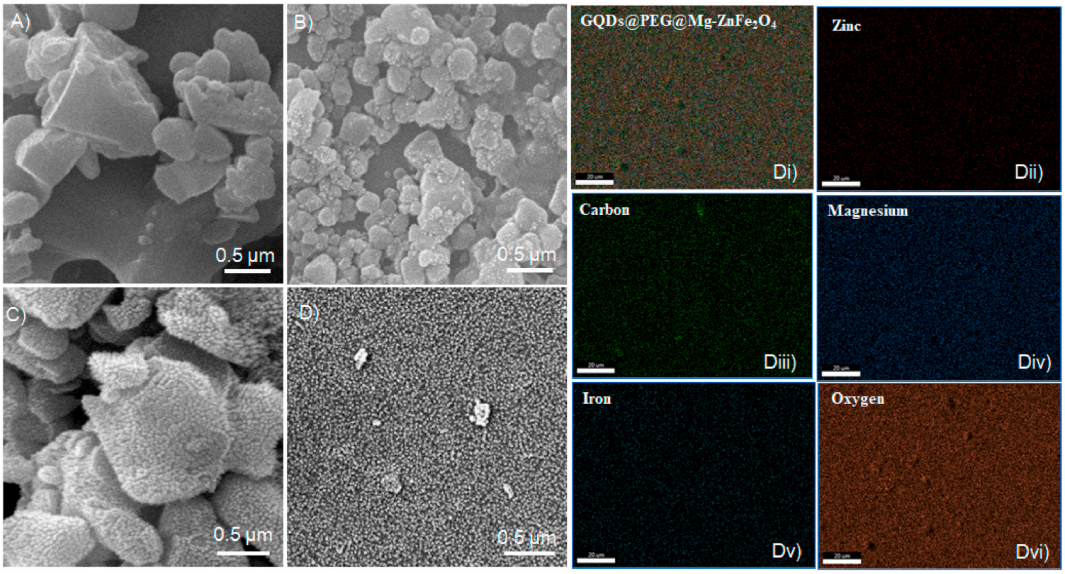

Fig. 3. SEM micrographs of (A) Mg–ZnFe$_2$O$_4$, (B) GQDs@Mg–ZnFe$_2$O$_4$, (C) PEG@Mg–ZnFe$_2$O$_4$, (D) GQDs@PEG@Mg–ZnFe$_2$O$_4$ and (Di-Dvi) Elemental mapping of ternary GQDs@PEG@Mg–ZnFe$_2$O$_4$ nanocomposite.

The lattice spacing d_{hkl} and its variation (Δd_{hkl}), incident X-ray wavelength (λ), crystallite shape factor (κ), crystallite size (D), and the angle of incidence of the X-ray beam (θ) are the factors involved in the determination of microstructural properties of materials. By analyzing the slope and intercept of the plot between $\frac{\beta \cos \theta}{\kappa\lambda}$ and $\frac{4 \sin \theta}{\kappa\lambda}$, the microstrain and crystallite size can be derived, which are given in Table 1. Fig. 2(B-E) depicts WH plots of Mg–ZnFe$_2$O$_4$, GQDs@Mg–ZnFe$_2$O$_4$, PEG@Mg–ZnFe$_2$O$_4$, and ternary GQDs@PEG@Mg–ZnFe$_2$O$_4$ nanocomposite, respectively.

The synthesized samples showed the average crystallite size (D) in the range of 10–43 nm. The highest D value was observed in Mg–ZnFe$_2$O$_4$ with a microstrain of $\sim 10^{-3}$. An increase in the crystallite size and microstrain was observed in binary GQDs@Mg–ZnFe$_2$O$_4$ nanocomposite, which can be attributed to the varied crystal growth dynamics upon the addition of GQDs, leading to the enhancement of crystal growth. The incorporation of PEG in PEG@Mg–ZnFe$_2$O$_4$ results in smaller crystallites due to the growth-inhibiting properties of PEG. The decreased microstrain of PEG@Mg–ZnFe$_2$O$_4$ compared to Mg–ZnFe$_2$O$_4$ might be due to the stabilizing nature of PEG. In ternary GQDs@PEG@Mg–ZnFe$_2$O$_4$ nanocomposites, the synergistic effect due to the addition of GQDs and PEG leads to a significant reduction in the crystallite size and microstrain.

The lattice parameter (a), interplanar spacing (d), unit cell volume (V), and X-ray density (d_X) was computed and presented in Table 1. The lattice parameter (a) of Mg–ZnFe$_2$O$_4$ showed a decreasing trend when compared to Mg–ZnFe$_2$O$_4$ in the binary and ternary nanocomposites. This decrease might be due to the interaction of GQDs and PEG molecules with Mg–ZnFe$_2$O$_4$. A similar trend was also observed in cell volume and X-ray density.

3.2. Fourier transform infrared spectroscopy (FTIR)

Fourier transform infrared (FTIR) was used to identify functional bonds; the data is shown in Fig. 2(F). FTIR spectra showed two distinct vibrational bands: ν_O and ν_T at 430 cm^{-1} and 565 cm^{-1} wavenumbers associated with metal ions vibrations at octahedral and tetrahedral sites, respectively [19]. The tetrahedral and octahedral voids are additionally known as A-site and B-site, respectively. The ν_O band showed lesser absorption due to weakly bonded Fe^{3+} ions at the B-site compared to the A-site. Furthermore, the existence of these vibrational bonds confirms the formation of the spinel structure of Mg–ZnFe$_2$O$_4$.

GQDs@Mg–ZnFe$_2$O$_4$ showed vibrational bands at 1360 cm^{-1} and 3430 cm^{-1} indicating the presence of –COOH and O–H functional groups in the GQDs, respectively. The spectra also exhibited vibration bands at 2950 cm^{-1} and 1350 cm^{-1} which corresponds to the stretching vibration of C–H and –COOH, which suggests that the nanocomposite contains some incompletely carbonized CA (citric acid) [22,23]. Furthermore, there is a vibration band at 1088 cm^{-1} that corresponds to the C–O–C group in the GQDs@Mg–ZnFe$_2$O$_4$. The FTIR spectra of PEG@Mg–ZnFe$_2$O$_4$ showed all the characteristic peaks of ferrites with an additional band of C–*O*–C at 1062 cm^{-1} as compared to Mg–ZnFe$_2$O$_4$ [24]. The FTIR spectrum of the ternary nanocomposite GQDs@PEG@Mg–ZnMg–ZnFe$_2$O$_4$ displays characteristic vibrational bands of the Mg–ZnFe$_2$O$_4$, GQDs, and PEG, indicating the presence of all three components in the ternary nanocomposite.

3.3. Scanning electron microscopy (SEM)

The morphological properties of all the samples were studied using a scanning electron microscope (SEM). The SEM images are

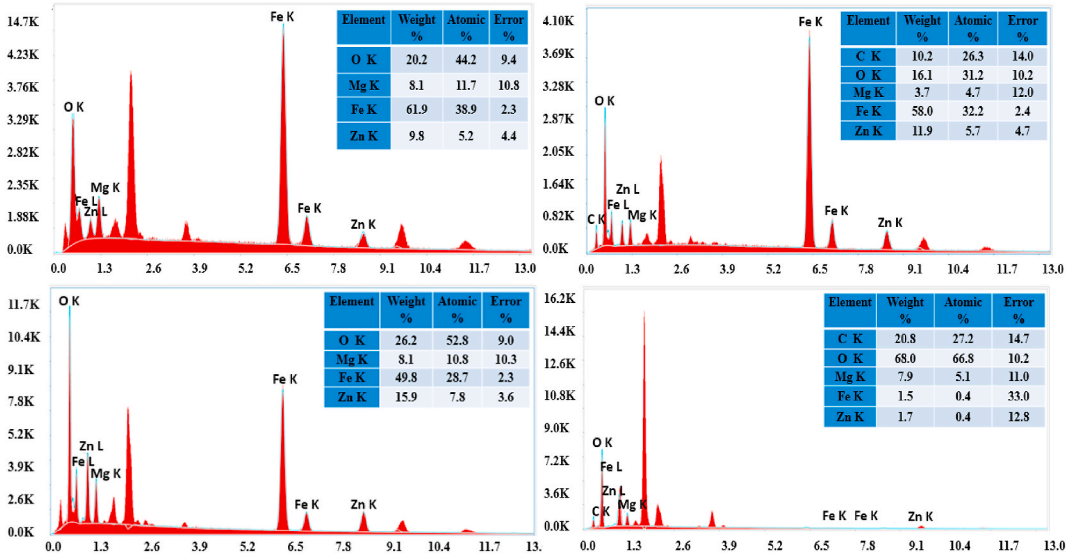

Element	Weight %	Atomic %	Error %
O K	20.2	44.2	9.4
Mg K	8.1	11.7	10.8
Fe K	61.9	38.9	2.3
Zn K	9.8	5.2	4.4

Element	Weight %	Atomic %	Error %
C K	10.2	26.3	14.0
O K	16.1	31.2	10.2
Mg K	3.7	4.7	12.0
Fe K	58.0	32.2	2.4
Zn K	11.9	5.7	4.7

Element	Weight %	Atomic %	Error %
O K	26.2	52.8	9.0
Mg K	8.1	10.8	10.3
Fe K	49.8	28.7	2.3
Zn K	15.9	7.8	3.6

Element	Weight %	Atomic %	Error %
C K	20.8	27.2	14.7
O K	68.0	66.8	10.2
Mg K	7.9	5.1	11.0
Fe K	1.5	0.4	33.0
Zn K	1.7	0.4	12.8

Fig. 4. EDX spectrum of (A) Mg–ZnFe_2O_4, (B) GQDs@Mg–ZnFe_2O_4, (C) PEG@Mg–ZnFe_2O_4, and (D) GQDs@PEG@Mg–ZnFe_2O_4 nanocomposites.

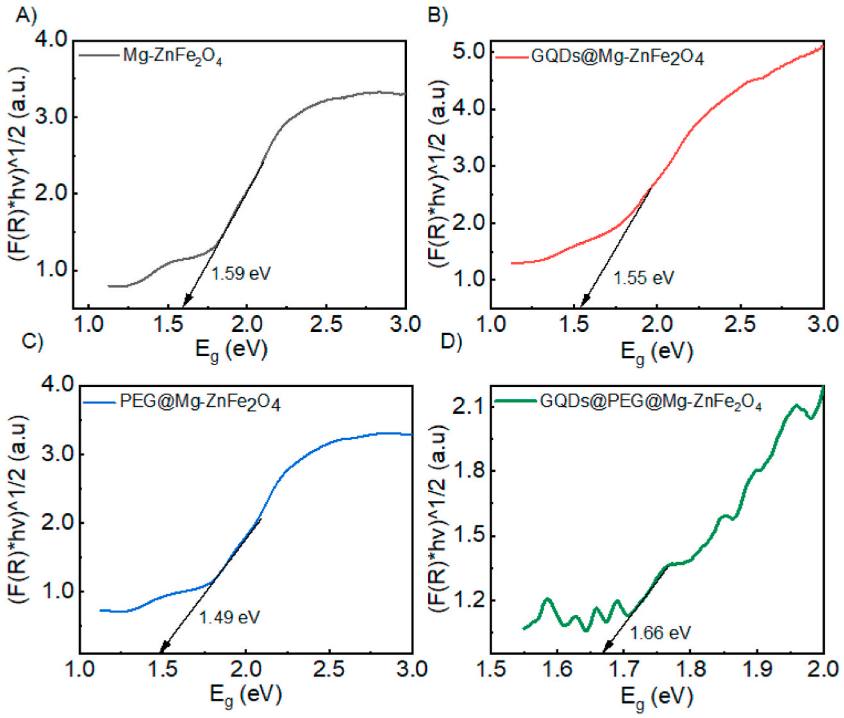

Fig. 5. KM-plots: (A) Mg–ZnFe_2O_4 (B) GQDs@Mg–ZnFe_2O_4 (C) PEG@Mg–ZnFe_2O_4 and (D) GQDs@PEG@Mg–ZnFe_2O_4 nanocomposites.

shown in Fig. 3(A-D). The SEM micrograph of Mg–ZnFe_2O_4 reveals the presence of large agglomerated particles, whereas, small spherical-shaped bright graphene quantum dots can be seen on the surface of GQDs@Mg–ZnFe_2O_4. The brightness of the GQDs is due to their good electrical conductivity. Similarly, uniform decoration of the Mg–ZnFe_2O_4 particles with small spherical PEG particles is evident in PEG@Mg–ZnFe_2O_4. A reduction in particle size of Mg–ZnFe_2O_4 as compared to binary and pristine was observed on GQDs@PEG@Mg–ZnFe_2O_4 nanocomposite. This reduction in size in the ternary composite can be attributed to the homogeneous dispersion of nanoparticles due to the presence of GQDs and PEG, which act as dispersants to prevent agglomeration. This is also in accordance with XRD results.

Elemental mapping is a technique used to visualize the spatial distribution of elements in a material. In the case of a ternary GQDs@PEG@Mg–ZnFe_2O_4 nanocomposite, the elemental mapping would show the distribution of magnesium, zinc, and iron in the

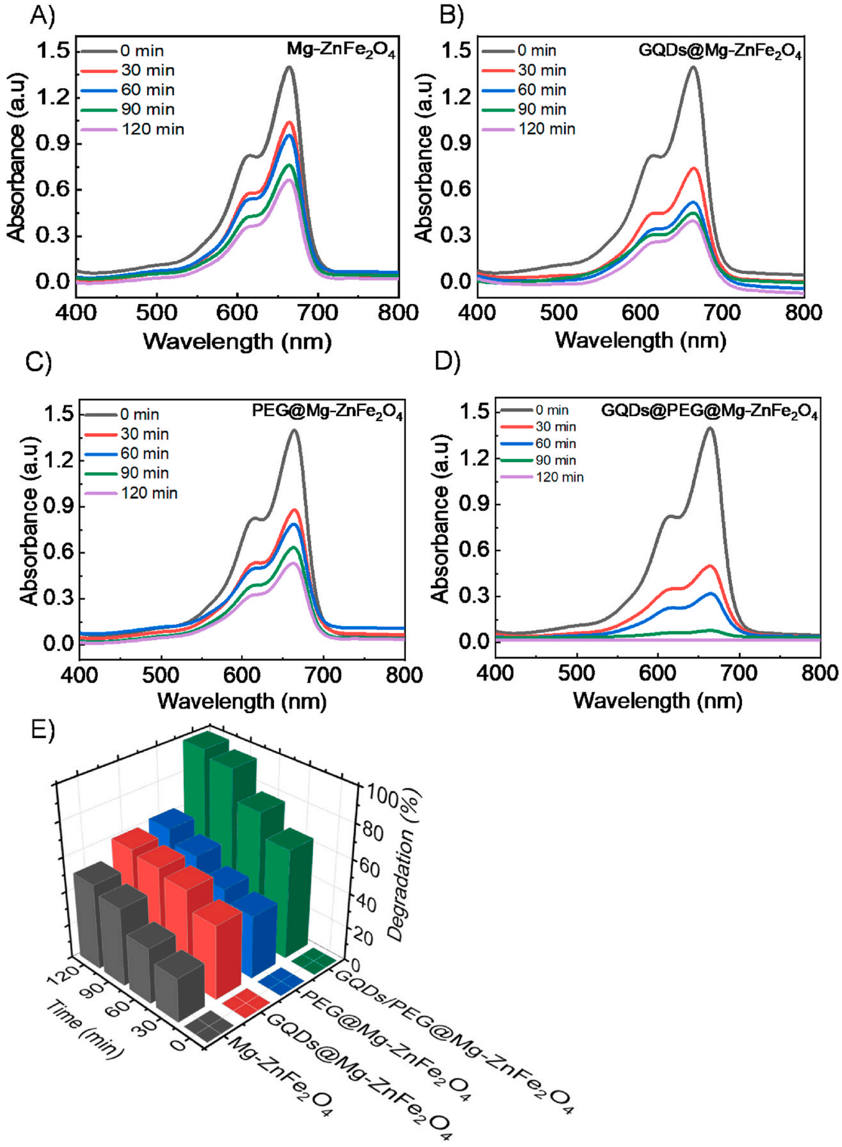

Fig. 6. (A–D) UV–visible absorption spectra of photodegradation of MB for Mg–ZnFe$_2$O$_4$, GQDs@Mg–ZnFe$_2$O$_4$, PEG@Mg–ZnFe$_2$O$_4$, GQDs@PEG@Mg–ZnFe$_2$O$_4$, nanocomposites and (E) degradation (%) for MB.

material as depicted in Fig. 3(Di-Dvi). The maps could be displayed in different colors, with each element assigned a specific color. By analyzing the maps, we observed a homogeneous distribution of each element in the composite material. The homogeneous distribution of elements in a material can lead to improved properties, such as improved electrical conductivity and increased thermal stability.

3.4. Energy dispersive X-ray spectroscopy (EDX)

EDX (Energy-dispersive X-ray spectroscopy) is performed to determine the elemental composition of all as-synthesized samples and their respective EDX spectrum. The results are shown in Fig. 4. EDX analysis depicts the presence of magnesium, zinc, iron, and oxygen in Mg–ZnFe$_2$O$_4$, GQDs@Mg–ZnFe$_2$O$_4$, PEG@Mg–ZnFe$_2$O$_4$, and GQDs@PEG@Mg–ZnFe$_2$O$_4$. Moreover, the increased concentration of carbon in GQDs@Mg–ZnFe$_2$O$_4$ and GQDs@PEG@Mg–ZnFe$_2$O$_4$ is because of GQDs and PEG.

3.5. Diffuse reflectance spectroscopy (DRS)

The bandgap of the prepared samples was calculated from the Kubelka–Munk (KM) plot by using the following equation

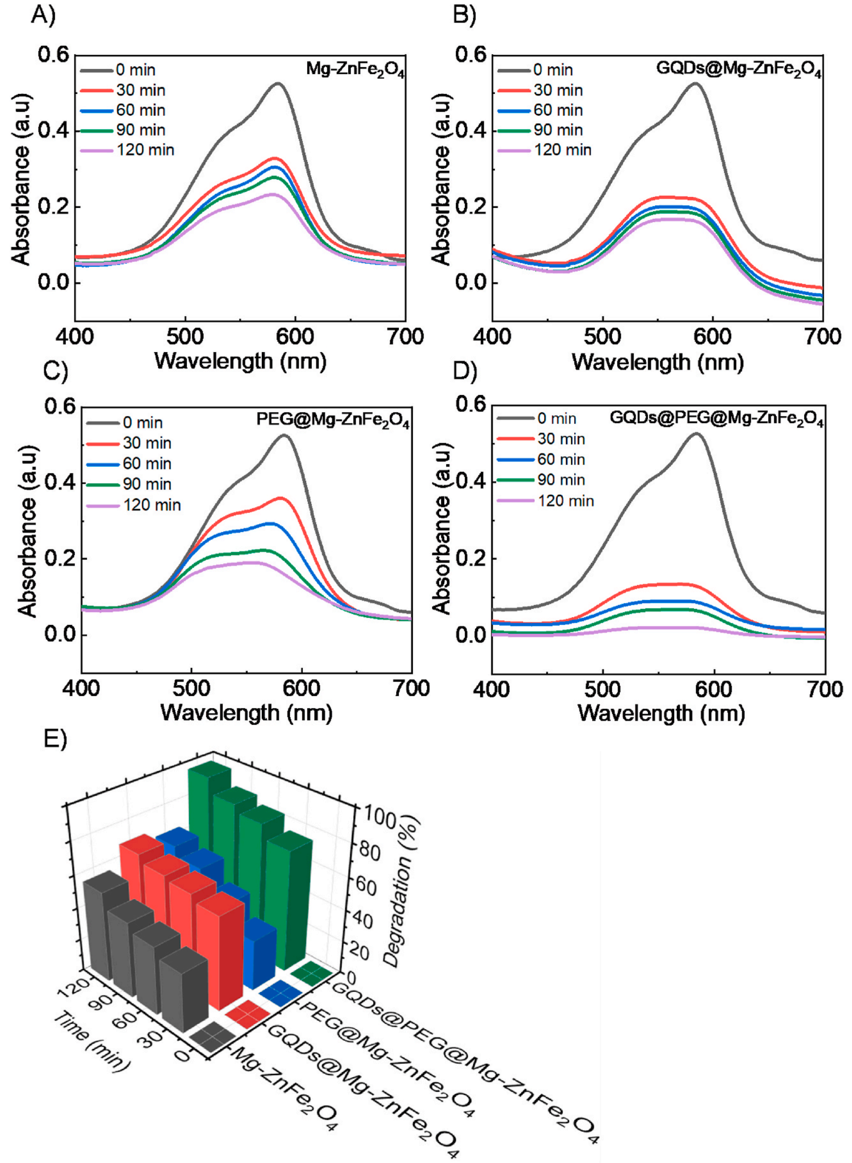

Fig. 7. (A–D) UV–visible absorption spectra of photodegradation of CV for Mg–ZnFe$_2$O$_4$, GQDs@Mg–ZnFe$_2$O$_4$, PEG@Mg–ZnFe$_2$O$_4$, GQDs@PEG@Mg–ZnFe$_2$O$_4$, nanocomposites and (E) degradation (%) for CV.

$$(F(R)h\nu)^n = A\,(h\nu - E_g) \tag{2}$$

Where $F(R)$ represents the KM function, h is the Planck constant, ν is the frequency of the incident photon, E_g is bandgap and the coefficient of absorption is A. $n = 1/2$ was used in all the samples as Mg–ZnFe$_2$O$_4$ is an indirect semiconductor. Fig. 5(A-D) presents KM-plot of Mg–ZnFe$_2$O$_4$, GQDs@Mg–ZnFe$_2$O$_4$, PEG@Mg–ZnFe$_2$O$_4$ and GQDs@PEG@Mg–ZnFe$_2$O$_4$ nanocomposites. Mg–ZnFe$_2$O$_4$ was found to have a bandgap energy of 1.59 eV, whereas a reduction in bandgap energy was observed in binary GQDs@Mg–ZnFe$_2$O$_4$ and PEG@Mg–ZnFe$_2$O$_4$ nanocomposites. This decrease in the band gap energy might be the consequence of new electronic states in the bandgap due to the addition of GQDs and PEG on the surface of Mg–ZnFe$_2$O$_4$. In contrast, the ternary GQDS@PEG@Mg–ZnFe$_2$O$_4$ nanocomposites showed an increase in bandgap energy compared to the Mg–ZnFe$_2$O$_4$ and binary nanocomposites. This could be attributed to the confinement of electrons and holes due to a reduction in the particle size upon the addition of graphene quantum dots (GQDs) and PEG as evident in the SEM results. Additionally, charge transfer between the GQDs/PEG and the Mg–ZnFe$_2$O$_4$ nanoparticles may result in electron occupation in lower-lying conduction band states. Moreover, the larger surface area of the ternary nanocomposite can contribute to the widening of the bandgap due to a higher density of surface states in the band gap [19].

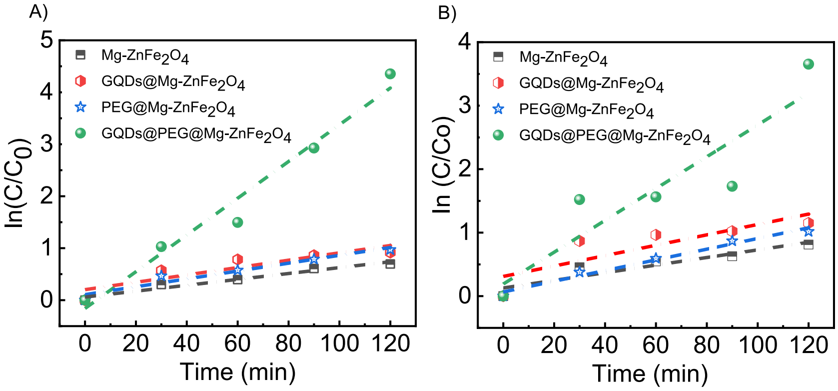

Fig. 8. Plot of ln (C/C_0) versus time for Mg–$ZnFe_2O_4$, GQDs@Mg–$ZnFe_2O_4$, PEG@Mg–$ZnFe_2O_4$, GQDs@PEG@Mg–$ZnFe_2O_4$, nanocomposites for (A) MB and (B) CV respectively.

3.6. *Photocatalytic properties*

Mg–$ZnFe_2O_4$ is a promising material for photocatalytic applications due to its unique properties such as high surface area, strong absorbance in visible light, and excellent stability. The effectiveness of Mg–$ZnFe_2O_4$ in degrading various organic dyes, including methylene blue (MB) and crystal violet (CV) was studied through a photocatalytic mechanism using sunlight. Fig. 6(A-D) shows UV–visible absorption spectra obtained at different times during the photodegradation process of MB using Mg–$ZnFe_2O_4$, GQDs@Mg–$ZnFe_2O_4$, PEG@Mg–$ZnFe_2O_4$ and GQDs@PEG@Mg–$ZnFe_2O_4$ as photocatalyst. The results show a reduction in the MB absorption spectra with degradation time in all the samples, indicating degradation of MB. The degradation efficiency was observed in the following order: GQDs@PEG@Mg–$ZnFe_2O_4$ > GQDs@Mg–$ZnFe_2O_4$ > PEG@Mg–$ZnFe_2O_4$ > Mg–$ZnFe_2O_4$. Fig. 6(E) presents degradation (%) as a function of degradation times for all the synthesized samples. The degradation efficiency showed a gradual increase, starting from 50 % for Mg–$ZnFe_2O_4$, progressing to ~60 % for the binary GQDs@Mg– $ZnFe_2O_4$ and PEG@Mg–$ZnFe_2O_4$ nanocomposites and reaching to above 98 % in ternary GQDs@PEG@Mg– $ZnFe_2O_4$ nanocomposite.

Fig. 7(A-D) shows the photodegradation of CV using Mg–$ZnFe_2O_4$, GQDs@Mg–$ZnFe_2O_4$, PEG@Mg–$ZnFe_2O_4$ and GQDs@PEG@Mg–$ZnFe_2O_4$ as photocatalyst. In all the samples, the results demonstrate a decrease in the CV absorption spectra with the passage of time, demonstrating its degradation. The order of the degradation efficiency was found to be the same as for MB. Furthermore, degradation (%) is shown in Fig. 7(E) at different degradation times for the prepared photocatalysts. The degradation efficiency increased gradually, from 55 % for Mg–$ZnFe_2O_4$ to 65 % for GQDs@Mg–$ZnFe_2O_4$ and PEG@Mg–$ZnFe_2O_4$ nanocomposites, and finally reaching above 97 % in ternary GQDs@PEG@Mg–$ZnFe_2O_4$ nanocomposite.

The mechanism of photocatalytic degradation of Mg–$ZnFe_2O_4$ involves a series of steps. Firstly, the molecules of the dye are absorbed onto the surface of the Mg–$ZnFe_2O_4$ particles through electrostatic and/or van der Waals interactions. The irradiation of sunlight leads to the transfer of electrons from the valence to the conduction band of Mg–$ZnFe_2O_4$, creating electron-hole pairs on the surface of these particles.

$$Mg - ZnFe_2O_4 + hv\ (sunlight) \rightarrow Mg - ZnFe_2O_4\ (e^- + h^+)$$

The excited electrons in the CB of the Mg–$ZnFe_2O_4$ react with adsorbed oxygen molecules and form superoxide radicals (O_2^-) whereas holes in the VB can oxidize the water molecules and result in the creation of hydroxyl radicals (OH*).

$$e^- + O_2 \rightarrow O_2^-$$

$$h^+ + H_2O \rightarrow OH^* + H^+$$

$$O_2^- + H^+ \rightarrow HO_2$$

$$HO_2 + e^- \rightarrow OH^*$$

These active radicals react with the adsorbed dye molecules and lead to their degradation. The degraded products of the dye molecules are further oxidized into smaller molecules such as carbon dioxide and water [25].

$$\left(HO_2, OH^*, O_2^-\right) + Dyes\ (Methylene\ Blue, Crystal\ Violet) \rightarrow Degradation\ products$$

The absorption spectra of binary GQDs@Mg–$ZnFe_2O_4$ and PEG@Mg–$ZnFe_2O_4$ nanocomposites depict an augmented degradation of dyes compared to Mg–$ZnFe_2O_4$ due to enhanced surface area and narrow bandgap [26]. The simultaneous presence of GQDs and PEG resulted in a significant reduction of particle size hence larger surface area which is a crucial factor in defining photocatalytic properties. Furthermore, the ternary nanocomposite showed a wider bandgap due to the presence of electrons in the conduction band. The enhanced electronic concentration in the conduction band promotes the formation of reactive oxygen species which results in the

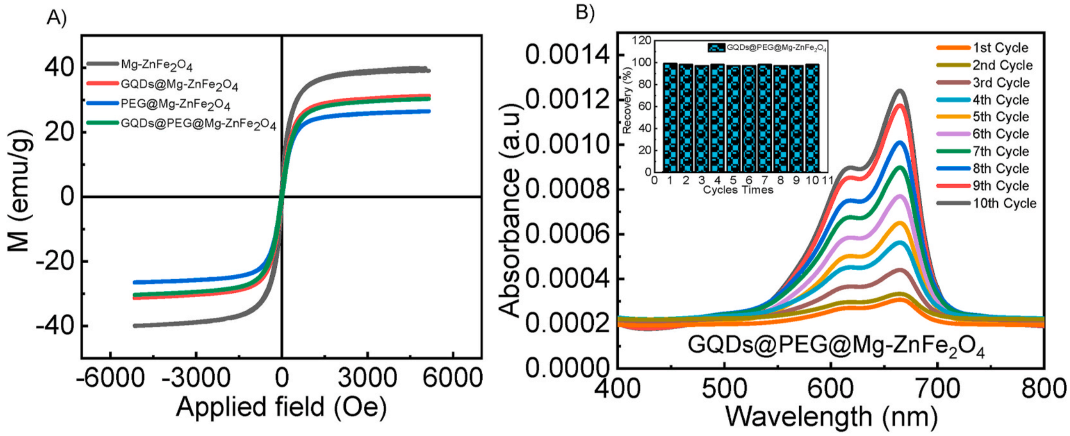

Fig. 9. (A) M − H curves of Mg–$ZnFe_2O_4$, GQDs@Mg–$ZnFe_2O_4$, PEG@Mg–$ZnFe_2O_4$, GQDs@PEG@Mg–$ZnFe_2O_4$ nanocomposites and (B) Recyclability plot of GQDs@PEG@Mg–$ZnFe_2O_4$ nanocomposite for 10 cycles; the inset in this figure shows magnetic recovery (%).

improvement of the photocatalytic activity of the ternary nanocomposite.

The degradation kinetics of the synthesized photocatalysts were estimated by the Langmuir–Hinshelwood kinetic model:

$$ln\left(\frac{C}{C_0}\right) = K_a t \tag{3}$$

In the equation, K_a represents the rate constant (min^{-1}), C_0 is the initial concentration (mg L^{-1}), and C is the concentration of the dye solution at time t (min). The results after fitting the model are shown in Fig. 8(A-B). The rate constants (K_a) were found in the following order: GQDs@PEG@Mg–$ZnFe_2O_4$ > PEG@Mg–$ZnFe_2O_4$ > GQDs@Mg–$ZnFe_2O_4$ > Mg–$ZnFe_2O_4$ photocatalyst. The highest rate constant for MB and CV was calculated to be 0.035 min^{-1} and 0.0258 min^{-1}, respectively, for the case when GQDs@PEG@Mg–$ZnFe_2O_4$ was used as the photocatalyst which is significantly higher than other photocatalysts. This indicates that the ternary nanocomposite possesses favorable characteristics for faster degradation of MB and CV under visible light. This finding is also consistent with the photocatalytic degradation result presented in Figs. 6 and 7.

3.7. Vibrating sample magnetometry (VSM)

VSM was used to study the magnetic behavior of the synthesized samples at room temperature with an applied magnetic field of ± 5 kOe. Fig. 9(A) shows the hysteresis behavior of Mg–$ZnFe_2O_4$, GQDs@Mg–$ZnFe_2O_4$, PEG@ Mg–$ZnFe_2O_4$, and GQDs@PEG@Mg–$ZnFe_2O_4$. The values of coercivity were calculated to be ~19 Oe for Mg–$ZnFe_2O_4$, ~16 Oe for GQDs@Mg–$ZnFe_2O_4$ and PEG@Mg–$ZnFe_2O_4$ nanocomposites, and ~15 Oe GQDs@PEG@Mg–$ZnFe_2O_4$ nanocomposite. All the samples showed superparamagnetic behavior indicating the presence of single magnetic domains. Mg–$ZnFe_2O_4$, GQDs@Mg–$ZnFe_2O_4$, PEG@Mg–$ZnFe_2O_4$, and GQDs@PEG@Mg–$ZnFe_2O_4$ showed a saturation magnetization (M_s) of 40 emu/g, 31 emu/g, 26 emu/g and 30 emu/g, respectively. In Mg–$ZnFe_2O_4$, Fe^{3+}, and Zn^{2+} ions are present at both A and B sites, while Mg^{2+} ions are located only on the B-site. The interaction between the tetrahedral and octahedral sub-lattices contributes to saturation magnetization. The lower saturation magnetization in GQDs@Mg–$ZnFe_2O_4$ and PEG@Mg–$ZnFe_2O_4$ nanocomposites is because of nonmagnetic GQDs and PEG.

For ternary GQDs@PEG@Mg–$ZnFe_2O_4$ nanocomposite, the obtained value of saturation magnetization is comparable with GQDs@Mg–$ZnFe_2O_4$ and it was found to be higher in contrast to PEG@Mg–$ZnFe_2O_4$. The observed enhancement in the saturation magnetization of ternary GQDs@PEG@Mg–$ZnFe_2O_4$ nanocomposite, besides the non-magnetic nature of GQDs and PEG, can be attributed to the fact that the simultaneous presence of GQDs, and PEG facilitates the redistribution of the Mg–$ZnFe_2O_4$ nanoparticles within the nanocomposite, resulting in a more uniform dispersion of magnetic moments leading to enhanced magnetic interactions [27]. This highlights the dual benefits of the synergistic effect of GQDs and PEG in enhancing both the magnetic properties and photocatalytic activity of the nanocomposite. Furthermore, it's worth noting that the ternary nanocomposite is magnetically separable, which facilitates easy collection and separation from the treated solution. The recyclability and magnetic recoverability of the GQDs@PEG@Mg–$ZnFe_2O_4$ were tested for 10 cycles for MB degradation and shown in Fig. 9(B). The nanocomposite showed comparable degradation efficiency for 10 cycles with an average recovery of 98 % by weight. Similar results were also obtained for the CV degradation for which the data is not shown here.

3.8. Evaluation of degraded products

To confirm the degradation of methylene blue and crystal violet, FTIR spectrum of the treated water was obtained and shown in Fig. 10(A). The obtained spectrum corresponds to that of pure water. No characteristic peak of the CV or MB was observed in the spectrum which is indicative of complete chemical degradation of the MB and CV in simpler compounds, such as carbon dioxide and

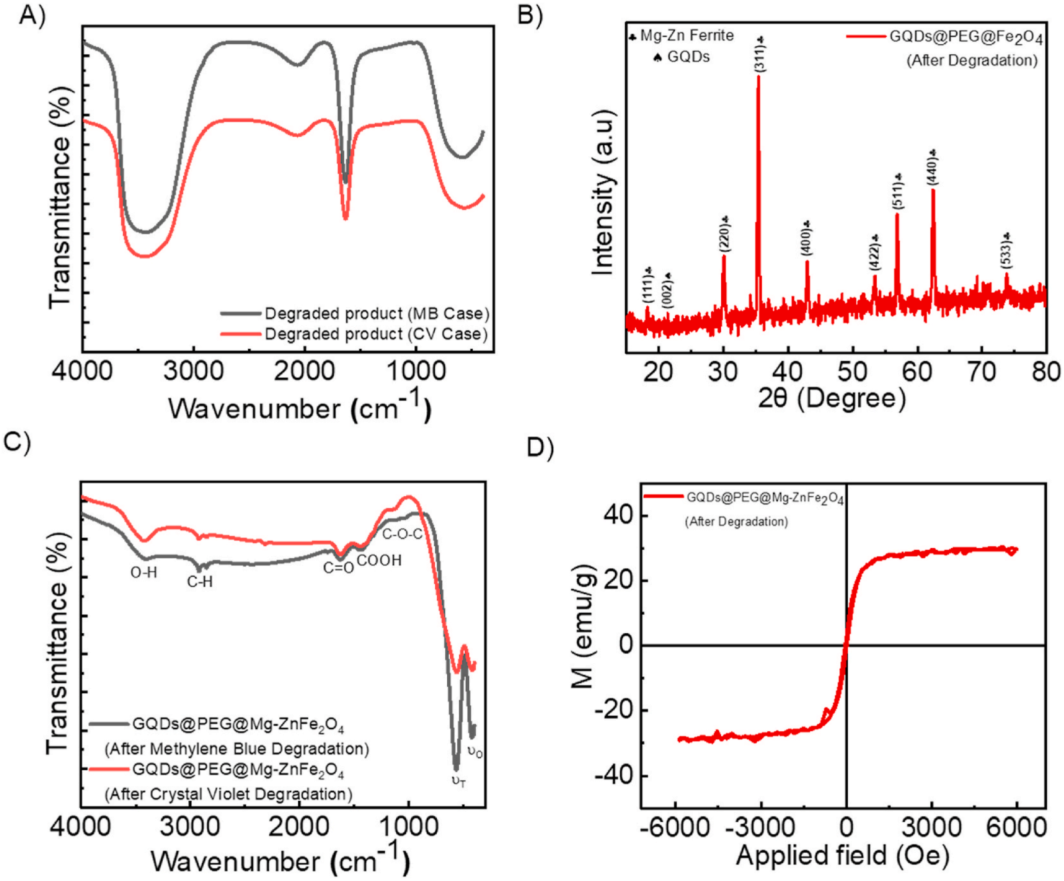

Fig. 10. (A) FTIR spectra of degraded product, (B) XRD, (C) FTIR, and (D) M − H curves of ternary GQDs@PEG@Mg–ZnFe$_2$O$_4$ nanocomposite after degradation reaction.

water [28,29].

3.9. Testing of photocatalyst after the degradation process

The structural stability of GQDs@PEG@Mg–ZnFe$_2$O$_4$ photocatalyst after the MB degradation process was investigated using XRD and data is shown in Fig. 10(B). All the peaks corresponding to as synthesized ternary GQDs@PEG@Mg–ZnFe$_2$O$_4$ nanocomposite can be seen, indicating no impact of the degradation process on the crystalline quality of the GQDs@PEG@Mg–ZnFe$_2$O$_4$. The FTIR spectra of GQDs@PEG@Mg–ZnFe$_2$O$_4$ after the photocatalytic degradation of methylene blue and crystal violet were also obtained and shown in Fig. 10(C). The existence of both ν_O and ν_T vibrational bands corresponding to Mg–ZnFe$_2$O$_4$ besides other vibrational bands related to GQDs and PEG are present, indicating no significant effect of the photocatalytic activity on the constituents of the nanocomposite. The morphology of GQDs@PEG@Mg–ZnFe$_2$O$_4$ photocatalyst, after the degradation process was examined through SEM and EDX. The micrographs, elemental composition, and elemental mapping are shown in Fig. 11(A-C). SEM micrographs showed similar structural morphology as compared to Fig. 3(D). The EDX analysis and elemental mapping confirmed the consistent homogeneous distribution of each element in the nanocomposite. These results indicate that the photocatalytic reaction did not induce significant morphological or compositional change after the degradation. These results collectively confirm the structural and chemical stability of the synthesized photocatalyst after the degradation process.

The magnetic property of GQDs@PEG@Mg–ZnFe$_2$O$_4$ photocatalyst, after the MB photocatalytic reaction was also investigated and shown in Fig. 10(D). The superparamagnetic behavior of the photocatalyst is evident with a saturation magnetization (M_s) of ~30 emu/g and coercivity of ~37 Oe. There is also a slight roughness in the data which can be attributed to the adsorption of the dyes on the surface of the photocatalyst. The retention of magnetic nature demonstrates that ternary GQDs@PEG@Mg–ZnFe$_2$O$_4$ nanocomposite is a potential photocatalyst for sustainable and cost-effective degradation of wastewater treatment.

4. Conclusion

In this study, the combination of XRD, FTIR, SEM, DRS, and VSM characterization techniques provided comprehensive insights into

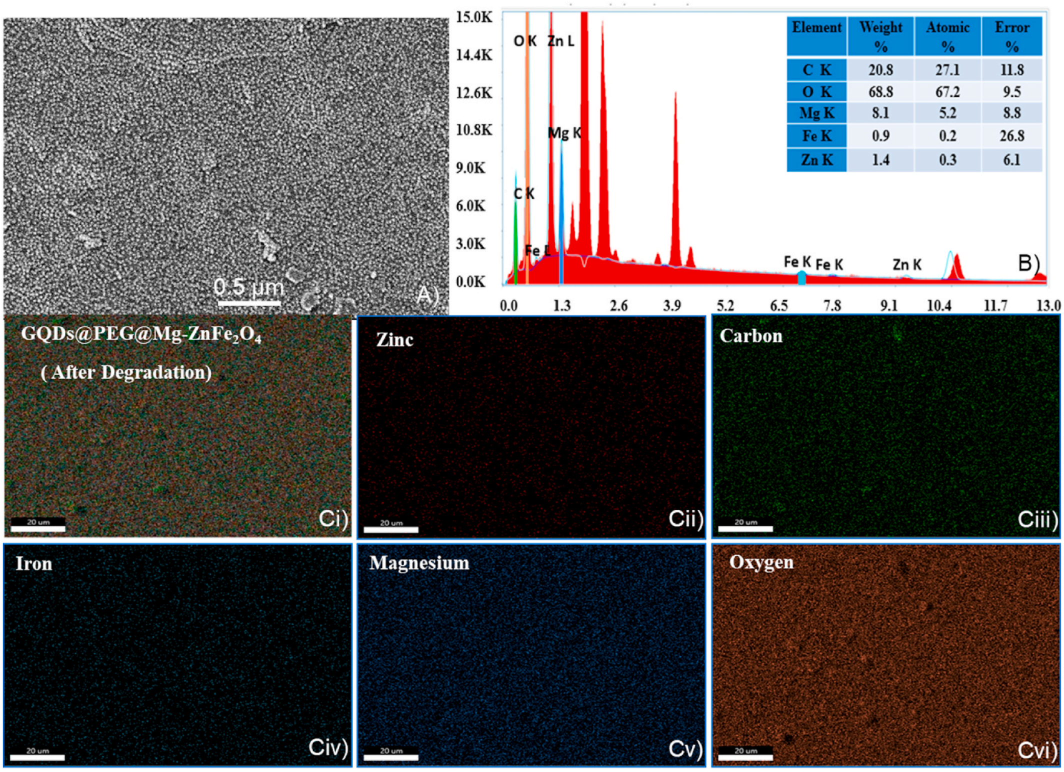

Element	Weight %	Atomic %	Error %
C K	20.8	27.1	11.8
O K	68.8	67.2	9.5
Mg K	8.1	5.2	8.8
Fe K	0.9	0.2	26.8
Zn K	1.4	0.3	6.1

Fig. 11. (A) SEM micrograph, (B) EDX and (Ci-Cvi) Elemental mapping of ternary GQDs@PEG@Mg–$ZnFe_2O_4$ nanocomposite after MB degradation reaction.

the structural, morphological, optical, and magnetic properties of the ternary GQDs@PEG@Mg–$ZnFe_2O_4$ nanocomposite. The XRD analysis confirmed the formation of the mixed spinel structure of the Mg–$ZnFe_2O_4$ along with the amorphous phase of GQDs and PEG without any impurity. The FTIR spectra confirmed Mg–$ZnFe_2O_4$, GQDs, and PEG presence in the nanocomposites. SEM micrographs disclosed that the synergistic effect of GQDs and PEG in the ternary nanocomposite resulted in the reduction of particle size. The bandgap study revealed excellent absorption ability of the nanocomposites in visible light which is beneficial for photocatalytic applications. The VSM analysis showed that the ternary GQDs@PEG@Mg–$ZnFe_2O_4$ nanocomposite exhibited comparable magnetic properties as compared to Mg–$ZnFe_2O_4$ which enabled magnetic recovery of ~98 % after the degradation process. GQDs@PEG@Mg–$ZnFe_2O_4$ nanocomposite proved to be an efficient photocatalyst for crystal violet (CV) and methylene blue (MB) degradation due to the synergistic effect of GQDs and PEG. Furthermore, GQDs@PEG@Mg–$ZnFe_2O_4$ nanocomposite was found to have structural and magnetic nature stability after the degradation process which provides insights into the use of the GQDs@PEG@Mg–$ZnFe_2O_4$ nanocomposites for the removal of dyes from textile industry waste on commercial scale.

CRediT authorship contribution statement

Saima Perveen: Writing – original draft, Data curation, Conceptualization. **Waheed Miran:** Visualization, Software, Data curation. **Gajanan Ghodake:** Writing – review & editing. **Waqar Azeem:** Writing – original draft. **Xizi Long:** Visualization, Investigation. **Fahad Azad:** Writing – review & editing, Writing – original draft, Supervision, Methodology, Formal analysis.

Declaration of generative AI and AI-assisted technologies in the writing process

During the preparation of this work, the author(s) used ChatGpt and QuillBot to improve language and readability only. After using this tool/service, the author(s) reviewed and edited the content as needed and take(s) full responsibility for the content of the publication.

Declaration of competing interest

The authors declare that they have no known competing financial interests or personal relationships that could have appeared to influence the work reported in this paper.

Acknowledgment

We thank SNS, NUST for the research grant and would like to extend our gratitude to IESE, NUST for their lab facilities.

References

[1] Y. Sun, Z. Lu, Y. Huang, Z. Qiu, H. Huang, C. Du, Study on the treatment of spraying wastewater from coal-fired flue gas by using discharge free radicals, J. Waste Disposal Sustain. Energy. 4 (2022) 231–242.
[2] A. Perebynos, D. Sepúlveda, C. Ribeiro, Study on textile waste generation in the undifferentiated municipal solid waste stream in Guimarães, Portugal, J. Waste Disposal Sustain. Energy 5 (2023) 189–203.
[3] T. Shen, M. Yan, Y. Xia, R. Hu, Y. Yang, C. Chen, F. Chen, D. Hantotoko, Treatment of wastewater from food waste hydrothermal carbonization via Fenton oxidization combined activated carbon adsorption, J. Waste Disposal Sustain. Energy 4 (2022) 205–218.
[4] V.L. Prasanna, V. Rajagopalan, A new Synergetic nanocomposite for dye degradation in dark and light, Sci. Rep. 6 (2016), 38606.
[5] K. Ravichandran, R. Shalini, M. Ayyanar, P. Kavitha, M. Baneto, M. Karunakaran, P.K. Praseetha, K.C.S. Pushpa, N. Anuradha, Effect of pH of the precursor solution on the photocatalytic and biomedical applications of enzyme coupled ZnO and SnO_2 nanomaterials: a comparative study, J. Water Process Eng. 53 (2023), 103817.
[6] K. Ancy, M.R. Bindhu, J.S. Bai, M.K. Gatasheh, A.A. Hatamleh, S. Ilavenil, Photocatalytic degradation of organic synthetic dyes and textile dyeing wastewater by Al and F co-doped TiO2 nanoparticles, J. Environ. Res. 206 (2022), 112492.
[7] S. Suvathi, R. Rathi, K. Ravichandran, P. Kavitha, M. Ayyanar, P.K. Praseetha, N. Chidhambaram, Improved photocatalytic dye degradation and seed germination through enzyme-coupled titanium oxide nanopowder - a cost-effective approach, J. Environ. Res. 218 (2023), 114973.
[8] M. Liu, Y. Ye, J. Ye, T. Gao, D. Wang, G. Chen, Z. Song, Recent advances of magnetite (Fe_3O_4)-based magnetic materials in catalytic applications, J. Magnetochem. 9 (2023) 110.
[9] A. Šutka, A.G. Kārlis, Spinel ferrite oxide semiconductor gas sensors, J. Sensors Actuat. B: Chemical. 222 (2016) 95–105.
[10] P. Liu, H. He, G. Wei, X. Liang, F. Qi, F. Tan, W. Tan, J. Zhu, R. Zhu, Effect of Mn substitution on the promoted formaldehyde oxidation over spinel ferrite: catalyst characterization, performance, and reaction mechanism, J. Appl. Catalysis B. 182 (2016) 476–484.
[11] S.F. Mansour, M.A. Abdo, Electrical modulus and dielectric behavior of Cr3+ substituted Mg–Zn nanoferrites, J. Magn. Magn Mater. 428 (2017) 300–305.
[12] K.K. Kefeni, B.M. Bhekie, A.M.M. Titus, Application of spinel ferrite nanoparticles in water and wastewater treatment: a review, J. Sep. Purif. Technol. 188 (2017) 399–422.
[13] A. Qu, H. Xie, X. Xu, Y. Zhang, S. Wen, Y. Cui, High quantum yield graphene quantum dots decorated TiO_2 nanotubes for enhancing photocatalytic activity, J. Appl. Surf. Sci. 375 (2016) 230–241.
[14] A. Sarwar, A. Razzaq, M. Zafar, I. Idrees, F. Rehman, W.Y. Kim, Copper tungstate (CuWO4)/graphene quantum dots (GQDs) composite photocatalyst for enhanced degradation of phenol under visible light irradiation, J. Results Phys. 45 (2023), 106253.
[15] M.S. Khan, N. Riaz, A.J. Shaikh, J.A. Shah, J. Hussain, M. Irshad, M.S. Awan, A. Syed, J. Kallerhoff, M. Arshad, M. Bilal, Graphene quantum dot and iron co-doped TiO2 photocatalysts: synthesis, performance evaluation and phytotoxicity studies, J. Ecotoxicol. Environm. Saf. 226 (2021), 112855.
[16] R. Tabit, O. Amadine, Y. Essamlali, K. Dânoun, A. Rhihil, M. Zahouily, Magnetic CoFe2O4 nanoparticles supported on graphene oxide (CoFe2O4/GO) with high catalytic activity for peroxymonosulfate activation and degradation of rhodamine B, J. RSC Adv. 8 (2018) 1351–1360.
[17] C. Yang, J. Du, Q. Peng, R. Qiao, W. Chen, C. Xu, Z. Shuai, M. Gao, Polyaniline/Fe3O4 nanoparticle composite: synthesis and reaction mechanism, J. Phys. Chem. B 113 (2009) 5052–5058.
[18] S. Rashid, S. Perveen, S. Hafeez, S.U. Asad, M.Z. Khan, F. Azad, Graphene quantum dots (GQDs) decorated Co-Zn ferrite: structural, morphological, dielectric, and magnetic properties, J. Magn. Magn Mater. 570 (2023), 170548.
[19] S. Perveen, S. Hafeez, S. Rashid, S.U. Asad, M.Z. Khan, F. Azad, A strategy to improve dielectric permittivity of Mg–Zn ferrite by using silver nanoparticles, J. Mater. Chem. Phys. 297 (2023), 127303.
[20] M.Z. Khan, G. Iftikhar, M.M. Baig, M.A. Akram, Facile synthesis of a multifunctional ternary SnO_2/MWCNTs/PANI nanocomposite: detailed analysis of dielectric, electrochemical, and water splitting applications, J. Electrochim. Acta 441 (2023), 141816.
[21] P.V. Ramana, K.S. Rao, K.H. Rao, Influence of iron content on the structural and magnetic properties of Ni-Zn ferrite nanoparticles synthesized by PEG assisted sol-gel method, J. Magn. Magn Mater. 465 (2018) 747–755.
[22] S. Ramachandran, M. Sathishkumar, N.K. Kothurkar, R. Senthilkumar, Synthesis and characterization of graphene quantum dots/cobalt ferrite nanocomposite, IOP Conf. Ser. Mater. Sci. Eng. 310 (2018), 012139.
[23] J. Diao, T. Wang, L. Li, Graphene quantum dots as nanoprobes for fluorescent detection of propofol in emulsions, J. R. Soc. Open Sci. 6 (2018), 181753.
[24] P.K. Roy, V. Swami, D. Kumar, C. Rajagopal, Removal of toxic metals using superabsorbent polyelectrolytic hydrogels, J. Appl. Polymer Sci. 122 (2011) 2415–2423.
[25] R. Sharma, P. Thakur, M. Kumar, P. Sharma, V. Sharma, Nanomaterials for high-frequency device and photocatalytic applications: Mg-Zn-Ni ferrites, J. Alloys Compounds 746 (2018) 532–539.
[26] R. Priya, S. Stanly, R. Anuradha & S. Sagadevan, "Evaluation of the photocatalytic activity of copper ferrite nanoparticles". J. Mater. Res. Express. 6(9), 095014.
[27] M.D. Mukadam, S.M. Yusuf, P. Sharma, S.K. Kulshreshtha, Particle size-dependent magnetic properties of γ-Fe_2O_3 nanoparticles, J. Magn. Magn Mater. 272–276 (2004) 1401–1403.
[28] A.A. Alshehri, M.A. Malik, Biogenic fabrication of ZnO nanoparticles using Trigonella foenum-graecum (Fenugreek) for proficient photocatalytic degradation of methylene blue under UV irradiation, J. Mater. Sci. Mater. Electron. 30 (2019) 6156–16173.
[29] Y. Cheng, F. Zhou, S. Li, Z. Chen, Removal of mixed contaminants, crystal violet, and heavy metal ions by using immobilized stains as the functional biomaterial, J. RSC Adv. 6 (2016) 67858–67865.